



HAL
open science

Diffusion MRI fiber orientation distribution function estimation using voxel-wise spherical U-net

Sara Sedlar, Théodore Papadopoulo, Rachid Deriche, Samuel Deslauriers-Gauthier

► **To cite this version:**

Sara Sedlar, Théodore Papadopoulo, Rachid Deriche, Samuel Deslauriers-Gauthier. Diffusion MRI fiber orientation distribution function estimation using voxel-wise spherical U-net. International MIC-CAI Workshop 2020 - Computational Diffusion MRI, Oct 2020, Lima, Peru. hal-02946371

HAL Id: hal-02946371

<https://hal.science/hal-02946371>

Submitted on 23 Sep 2020

HAL is a multi-disciplinary open access archive for the deposit and dissemination of scientific research documents, whether they are published or not. The documents may come from teaching and research institutions in France or abroad, or from public or private research centers.

L'archive ouverte pluridisciplinaire **HAL**, est destinée au dépôt et à la diffusion de documents scientifiques de niveau recherche, publiés ou non, émanant des établissements d'enseignement et de recherche français ou étrangers, des laboratoires publics ou privés.

Diffusion MRI fiber orientation distribution function estimation using voxel-wise spherical U-net

Sara Sedlar, Théodore Papadopoulo, Rachid Deriche, and Samuel Deslauriers-Gauthier

Inria Sophia Antipolis-Méditerranée, Université Côte d’Azur, FR
Athena Project-Team

Abstract. Diffusion Magnetic Resonance Imaging (dMRI) is an imaging technique which enables analysis of the brain tissue at a microscopic scale, particularly the analysis of white matter. Given a high enough angular resolution, a common way to explain the measured signal is via fiber orientation distribution function (fODF). This function describes the orientation and volume fraction of axon bundles within each voxel and is an essential ingredient of tractography. In this work, we have investigated a deep learning approach for the fODF estimation. U-nets enable fast and high resolution inference by combining multi-scale features from contracting and expanding parts of the network. As dMRI signals are most commonly acquired on spheres, we propose a spherical U-net which is adjusted to the properties of the dMRI data, namely its real nature, antipodal symmetry, uniform sampling and axial symmetry of the signals corresponding to individual fibers. We compared our model with another deep learning approach based on a 3D convolutional neural network and a state-of-the-art approach - multi-shell multi-tissue constrained spherical deconvolution, on real data from Human Connectome Project and synthetic data generated using ball and stick model. The methods are compared in terms of mean square error and mean angular error for dMRI signals of different angular resolutions. Provided quantitative analyses show improved performance with our approach even with significantly reduced number of parameters and results obtained on synthetic data indicate its robustness with respect to noise. Qualitative results illustrating the performance of the methods are also presented.

Keywords: diffusion MRI · fiber orientation distribution function · spherical U-net

1 Introduction

Diffusion MRI is an imaging modality tailored to capture interactions of diffusing water molecules with surrounding micro-structures within examined tissue. As such, it has shown importance in neuroimaging, particularly in the analysis of white matter micro-structures. It opened the possibility to examine properties of axon bundles such as orientation, volume fraction, dispersion, etc. Models

proposed to explain the dMRI signals have evolved with the improvement of the acquisition process. Initially, in Diffusion Tensor Imaging [1], axon bundles were described via diffusion tensors [2]. With the increase of dMRI angular resolution, more informative models have been proposed, specifically in voxels containing crossing or kissing fibers, fiber fanning or bending. A number of these models include estimation of probability density functions (PDF) such as Ensemble Average Propagator (EAP) [3,4] describing average relative spin displacements, diffusion Orientation Distribution Function (dODF) [5,6] and fiber Orientation Distribution Function (fODF) [7,8,9]. These voxel-wise quantities opened the possibility of tracking white matter pathways - tractography [10], a process of a great potential in the analysis of brain structural connectivity [11].

The fODF is a spherical PDF that reveals orientations and volumes of the underlying axon bundles. Traditional methods include estimation of a single fiber response function that is deconvolved from the dMRI signal in order to obtain the fODF [7,8,9].

Recently, a 3D convolutional neural network (3DCNN) directly applied on spherical harmonic (SH) coefficients has been proposed for the fast estimation of fODFs [12]. In [13], for the same problem, residual CNN (ResCNN) and dense neural network (ResDNN) have been investigated. In both works, potential of the models has been demonstrated for significantly downsampled acquisition sampling schemes, what is often a requirement in clinical applications.

U-nets have shown potential in high resolution inference from planar data by combining multi-scale features from contracting and expanding parts of the network [14]. As sampling of dMRI signals is most commonly performed on spheres, all building blocks of U-net need to be adjusted to the properties of spherical signals. Recently, in [15], a spherical U-net has been proposed for the cortical surface parcellation and prediction of attribute maps, with convolutions, pooling and transposed convolutions adjusted to the spherical space. A neural network model, similar to the planar CNN, for the analysis of spherical data - spherical CNN (S^2CNN) has been introduced in [16], where, contrary to [15], in order to avoid computationally expensive interpolations, convolutions of signals and kernels are performed in spectral domain. Similar approach has been developed in [17], where a significant speed up of convolutions has been achieved with zonal kernels.

In this work, we have addressed the problem of the fODF estimation from dMRI data acquired with significantly downsampled acquisition schemes. Exploiting the properties of the *U-net* and S^2CNN , we propose a voxel-wise spherical U-net, that is tailored to the properties of dMRI signals acquired on spheres, namely real nature, uniform distribution of samples, antipodal and axial symmetry of the signals generated by individual fibers.

2 Background and method

The main operations in U-nets are convolutions, pooling, and transposed convolutions. While the convolution of equidistantly discretized planar signals with

kernels is well defined, convolution between S^2 signals and kernels faces two challenges. First of all, the operation analogue to the translation in Euclidean space during convolution is not a rotation in S^2 space, but in the $SO(3)$ manifold. Secondly, the discretization of signals in Euclidean space is usually done in an equidistant manner, what cannot be achieved in S^2 domain. An interpolation must therefore be performed for each step of convolution. These problems are addressed in the work presented in [16] where the spherical CNN - S^2CNN has been introduced. In this framework, to avoid the computationally expensive interpolations, convolutions of S^2 and $SO(3)$ signals and kernels are performed in spectral domain, and as in standard CNNs, activation function is applied in signal domain. Furthermore, to achieve the same effect as pooling, in each new layer, the bandwidth of the input signal is reduced and the support of the kernel is spread. In [17], additional speed up has been achieved by constraining kernels to be zonal. As a consequence, the convolution can be more efficiently performed in S^2 . In this work, we propose a spherical U-net with convolutional building blocks from [16,17] adjusted to the properties of dMRI data.

Given the antipodal symmetry of the dMRI signals, we use only the SH basis of even degree for their representation. A signal $s : (\theta, \phi) \rightarrow R$ can be written as

$$s(\theta, \phi) = \sum_{l=0}^{L_{max}} \sum_{m=-l}^{m=l} \hat{s}_l^m Y_l^m(\theta, \phi), \text{ for } l \in \{0, 2, \dots, L_{max}\} \quad (1)$$

where θ and ϕ are inclination and azimuth angles, $Y_l^m(\theta, \phi)$ are SH basis of order m and degree l , and \hat{s}_l^m are the corresponding SH coefficients. L_{max} is the signal's bandwidth determined as

$$N \geq (L_{max} + 1)(L_{max} + 2)/2 \quad (2)$$

where N is the number of sampling points. In addition, as dMRI signals are real, we reduce computational complexity by using the real SH basis

$$Y_{lm} = \begin{cases} \sqrt{2}(-1)^m \text{Im}[Y_l^{|m|}] & \text{if } m < 0 \\ Y_l^0 & \text{if } m = 0 \\ \sqrt{2}(-1)^m \text{Re}[Y_l^m] & \text{if } m > 0 \end{cases} \quad (3)$$

Consequently, spherical kernels are also real and antipodally symmetric. Another important property of dMRI signals is the axial symmetry of the signals coming from individual axon bundles. This motivated us to use kernels that are axially symmetric around z axis - zonal kernels and in this way promote an axon bundle-wise feature extraction. Zonal kernels have been introduced in [17] in order to decrease the computational complexity imposed by performing convolutions of $SO(3)$ signals and kernels as in [16]. Given this, kernel $h : (\theta) \rightarrow R$ can be represented as a linear combination of zonal harmonics (ZH) as

$$h(\theta) = \sum_{l=0}^{L_{max}} \hat{h}_l Y_l^0(\theta, 0), \text{ for } l \in \{0, 2, \dots, L_{max}\}. \quad (4)$$

This significantly simplifies convolution between signals and kernels, as the resulting signal is no longer in $SO(3)$ manifold, but in S^2 space. In addition, since the number of ZHs necessary to represent such kernels is rather small - $L_{max}/2 + 1$, we used directly ZH coefficients as trainable parameters as it was initially introduced in [17]. Convolution between a signal $s : (\theta, \phi) \rightarrow R$ and an axially symmetric kernel $h : (\theta) \rightarrow R$, represented with ZH coefficients \hat{h}_l can be written as

$$c(\theta, \phi) = \sum_{l=0}^{L_{max}} \hat{h}_l \sum_{m=-l}^{m=l} \hat{s}_l^m Y_l^m(\theta, \phi), \text{ for } l \in \{0, 2, \dots, L_{max}\}. \quad (5)$$

As we are dealing with discrete signals, Eq. 1 can be simply written as matrix-vector product as $\mathbf{s} = Y \hat{\mathbf{s}}$, where Y contains SH basis $Y_l^m(\theta_k, \phi_k)$ in columns, sampled at the angles (θ_k, ϕ_k) , $\hat{\mathbf{s}}$ are corresponding SH coefficients and \mathbf{s} is a discrete spherical signal. Although the discretization of the band-limited planar signals without information loss is well defined with Nyquist-Shannon sampling theorem and their transformation to spectral domain is trivial, discretization of the spherical signals and calculation/estimation of SH coefficients is a challenging task. Sampling theorem for band-limited spherical signals has been introduced in the work of Driscoll and Healy [18], where they have defined an equiangular sampling grid that guarantees information preservation and calculation of SH coefficients. The total number of required samples is $N = 4(L_{max} + 1)^2$. Given a signal sampled on Driscoll-Healy grid, $\mathbf{s} : (\theta_k, \phi_k) \rightarrow R$ and SH basis discretized in the same way in a matrix Y , calculation of SH coefficients can be simply written as $\hat{\mathbf{s}} = WY^H \mathbf{s}$, where H refers to conjugate transpose and W are quadrature weights necessary to account for the basis orthogonality loss due to discretization. This sampling is quite excessive and given a real world situation where a signal is not completely band-limited and is affected by noise, signal segments around poles that are oversampled would be more accurately represented. Due to this, sampling on a sphere is, in general, application dependent and dMRI signals are usually sampled uniformly over multiple shells in a way that an optimal angular coverage is achieved [28]. As a consequence, some information can be lost and several methods for the estimation of SH coefficients have been proposed [19,20,21]. In this work, we have used Gram-Schmidt orthonormalization process to estimate the basis Y' for the transformation of S^2 signals into spectral domain, similarly as introduced by Yeo [19]. This is performed in an iterative manner, if y_i and y'_i correspond to i -th columns of Y and Y' , respectively, y'_i are determined as follows:

$$y'_i = y_i - \sum_{j=0}^{i-1} \frac{\langle y_i, y'_j \rangle}{\langle y'_j, y'_j \rangle} y'_j, \quad y'_i = \frac{y'_i}{\|y'_i\|_2}. \quad (6)$$

where $y'_0 = y_0$. In this iterative process, as we start from basis that correspond to lower frequencies, more importance is given to them. This is convenient as we know that aliasing affects higher frequencies. In order to avoid bias due to ordering of the basis, Gram-Schmidt process is repeated multiple times, each

time randomly shuffling the order of the basis of the same degree, which are at the end averaged. SH coefficients are simply estimated as $\hat{\mathbf{s}} = Y'^T \mathbf{s}$.

Voxel-wise spherical U-net Figure 1 depicts an illustration of the proposed spherical U-net. Input to the U-net is composed of $n^3 \cdot n_{shells}$ discrete S^2 channels, where n is the size of neighbourhood and n_{shells} is the number of dMRI shells. Output corresponds to the SH coefficients of the estimated fODF. We refer to the results of (transposed) convolution of input S^2 signals and zonal kernels, followed by activation function, as *feature maps*, which are sampled at uniformly distributed points on sphere, generated using *Q-sampling tool* [28]. The network is composed of contracting and expanding parts. Each layer of the contracting part extracts feature maps that are of the same bandwidth as its input (that is used as a part of the input to the parallel layer in the expanding part, black horizontal arrows in Figure 1) and corresponding feature maps with decreased bandwidth that serve as the input to the following layer of the contracting part (pink arrows oriented down in Figure 1). The decrease in bandwidth imitates pooling of the planar CNNs. Feature maps of the same bandwidth are computed as convolution of signals/feature maps transformed into spectral domain and kernels, represented with ZH coefficients, as in Eq. 5, followed by Rectified Linear Unit (ReLU) activation function. These feature maps are further transformed into spectral domain with decreased bandwidth and serves as the input to the following layer of the contracting part. Each layer of the expanding part learns up-sampling of the feature maps which serve as the input to the following layer in the expanding chain or as the final inference. In general, as input, it receives the feature maps from the parallel layer of the contracting part, if such layer exists (black horizontal arrows in Figure 1) and the feature maps estimated by the previous layer of the expanding part (turquoise arrows oriented up in Figure 1). Transposed convolution in planar CNN simply corresponds to the insertion of zeros between points and convolution with kernels. We have implemented the transposed convolution as follows

- Let N_i be the number of sampling points of the input feature maps of layer i with bandwidth L_{max}^i determined according to inequality 2.
- To up-sample the feature maps from layer i to layer $i - 1$ to have bandwidth $L_{max}^{(i-1)}$, we first generate N_{i-1} sampling points using *Q-space sampling tool* [28] and compute the corresponding basis Y' as in Eq. 6.
- Since Q-space sampling points are generated incrementally, positions of the points of the layer i correspond to the first N_i points of the sampling scheme of the layer $i - 1$, so inserted zeros correspond to the last $N_{i-1} - N_i$ points.
- Up-sampled SH coefficients are computed as $\hat{\mathbf{s}}_{i-1} = Y'_{:,1:N_i}{}^T \mathbf{s}_i$, where $:, 1 : N_i$ refers to the cropping of the matrix Y'^T to N_i columns.
- Convolution of the up-sampled signals and kernels is performed as in Eq. 5 followed by an activation function.

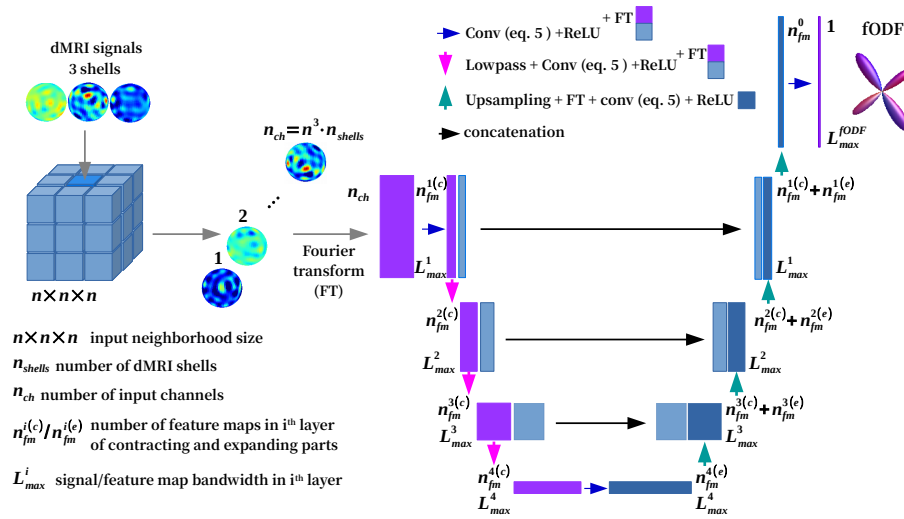


Fig. 1. Illustration of a spherical U-net architecture with corresponding convolutional operations in contracting and expanding parts

3 Dataset

We used in our experiments two types of datasets, real data from Human Connectome Project (HCP) [22] (referred to as *Real dataset*) and synthetic data generated from the same real HCP scans using multi-fiber ball and stick biophysical model [23] following the procedure described in [24]. Real data was acquired on Siemens 3T Skyra system with 100 mT /m gradient, over three shells with b-values of 1000, 2000 and 3000 s/mm^2 , each with 90 gradient directions and 18 b = 0 images at resolution 1.25x1.25x1.25 mm^3 . To generate synthetic data, first, up to three fiber orientations and corresponding volume fractions were estimated per voxel using the *bedpostx* tool from the *FSL* library [25]. These parameters were then used to generate synthetic data using the multi-fiber ball and stick model as in [24] for each shell independently. In the generation process, the free diffusivity coefficients are set to $\{0.68, 0.96, 2.25\} \cdot 10^{-3} s/mm^2$ for the white matter, gray matter and cerebrospinal fluid, respectively [24]. Single-fiber tensor's eigenvalues are set to $\{\lambda_1, \lambda_2, \lambda_3\} = \{1.7, 0.17, 0.17\} \cdot 10^{-3} s/mm^2$ [24]. To simulate more realistic dMRI data, Rician noise with SNR=18 was added to the synthesized data. In addition, in order to investigate the robustness of the compared methods, one synthetic dataset is generated with the constant diffusion single-fiber tensor eigenvalues (*Synthetic dataset 1*) as in [24] and another one with the eigenvalues taken from the uniform distribution around these values (values taken from the range of $\pm 10\%$) (*Synthetic dataset 2*). Experiments are conducted on *Real dataset*, *Synthetic dataset 1* and *Synthetic dataset 2* with downsampled acquisition schemes. To select relevant white matter voxels, we used brain tissue segmentation computed from T1w images using the *FAST* al-

gorithm [26] implemented in the *mrtrix* library [27]. Gold standard fODFs, of SH degree 8, were estimated using the multi-shell multi-color constrained spherical deconvolution (MSMT-CSD) approach [9], on signals acquired on full sampling scheme, using *mrtrix* library [27]. In the case of synthetic data, fODFs were estimated on the noise-less data. We used 50 subjects in total, 30 for training, 10 for validation and 10 for testing.

4 Experiments and implementation details

In order to evaluate our method on data similar to those used in clinical practice, experiments are performed on data with significantly reduced number of sampling points N_p (20, 30, 40, 60, 90 and 120 in total for the three shells). We compared our method with another deep learning approach - 3DCNN [12] and with MSMT-CSD [9]. To investigate importance of neighbourhood information, our model is trained with single voxel multi-shell ($S^2U-net^{1 \times 1 \times 1}$) signals and with $3 \times 3 \times 3$ neighbourhood multi-shell input ($S^2U-net^{3 \times 3 \times 3}$), what is also the case with the 3DCNN model. In addition, to investigate potential of our approach, we trained one model with significantly lower number of trainable parameters - $S^2U-net_s^{3 \times 3 \times 3}$. Sizes of the deep learning networks are given in Table 1. Both deep learning approaches are implemented using the *tensorflow* library

Table 1. Sizes of 3DCNNs and S^2U -nets (MB) for N_p sampling points.

Model / N_p	20	30	40	60	90	120
3DCNN	18.12	18.12	18.12	18.96	20.18	20.18
$S^2U-net^{1 \times 1 \times 1}$	15.65	15.65	15.65	19.30	20.52	20.52
$S^2U-net_s^{3 \times 3 \times 3}$	3.99	3.99	3.99	4.89	5.17	5.17
$S^2U-net^{3 \times 3 \times 3}$	15.80	15.80	15.80	19.42	20.60	20.60

[29]. Models are trained over 100 epochs. In each epoch, 3 dMRI samples are randomly selected from 30 training samples. For both models loss function is defined as mean square error (MSE) between estimated and gold standard fODFs represented in spectral domain. Initial learning rate is 0.001 and after 50 epochs it is reduced to 0.0001. Model weights updates are computed using the Adam optimization algorithm [30].

5 Results and conclusions

Results are compared quantitatively in terms of MSE and mean angular error (MAE) for single fiber voxels and voxels containing two crossing fibers. To compute peaks of the estimated and gold standard fODFs we used the *mrtrix* library [27] and the threshold of 0.1 of the highest peak is used to eliminate spurious fibers. In Figure 2 we can see that our models $S^2U-net^{3 \times 3 \times 3}$ achieve

significantly lower MSE compared to the models that do not use neighbouring information and slightly, but consistently lower MSE compared to $3DCNN$. In addition, almost equal performance can be achieved with a more compact model - $S^2U-net_s^{3 \times 3 \times 3}$. In Figure 3 we can notice that for single fiber voxels and real dataset, MAE is almost equal to the one achieved with MSMT-CSD, however the results obtained on synthetic data indicate that our approach is more robust to noise. As depicted in Figure 3, $S^2U-net^{3 \times 3 \times 3}$ and $S^2U-net_s^{3 \times 3 \times 3}$ achieve lower MAE in voxels with crossing fibers. Qualitative comparison of MSMT-CSD, $3DCNN$ and $S^2U-net^{3 \times 3 \times 3}$ is provided in Figure 4 for 60 sampling points. We can notice that MSMT-CSD compared to the $3DCNN$ and $S^2U-net^{3 \times 3 \times 3}$ is more prone to produce spurious fibers, while these deep learning approaches are more likely to omit some.

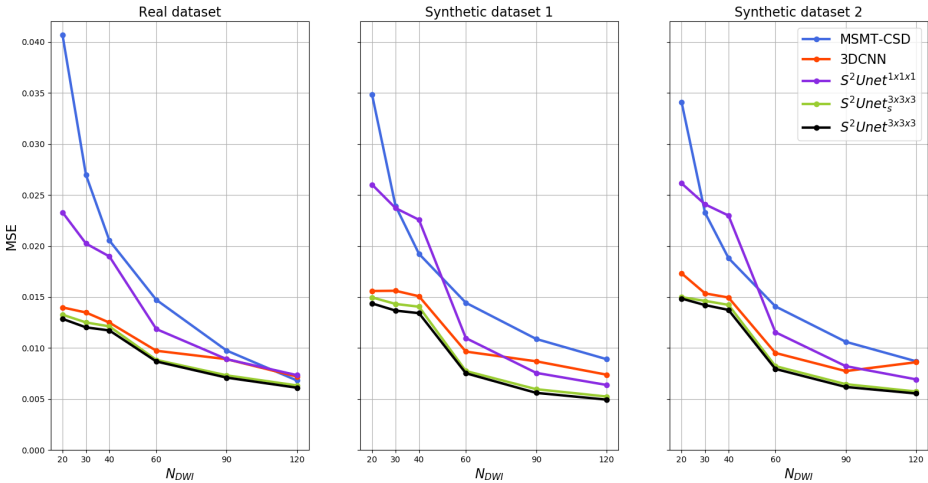


Fig. 2. Comparison of MSE averaged over 10 testing subjects for *real HCP dataset*, *Synthetic dataset 1* and *Synthetic dataset 2* for different number of sampling points.

In this work we have proposed a deep learning method that is adjusted to the properties of dMRI signals, namely real and spherical nature of the signals, antipodal symmetry, random distribution of the sampling points and axial symmetry of signals coming from individual fibers. We have demonstrated that the proposed method is suitable for high resolution inference such as the estimation of the fODFs and can successfully incorporate neighbouring information to boost its performance. Compared with the $3DCNN$, the method is capable to produce better fODF estimates even with a significantly reduced number of parameters. Results obtained on synthetic data indicate a better robustness with respect to noise.

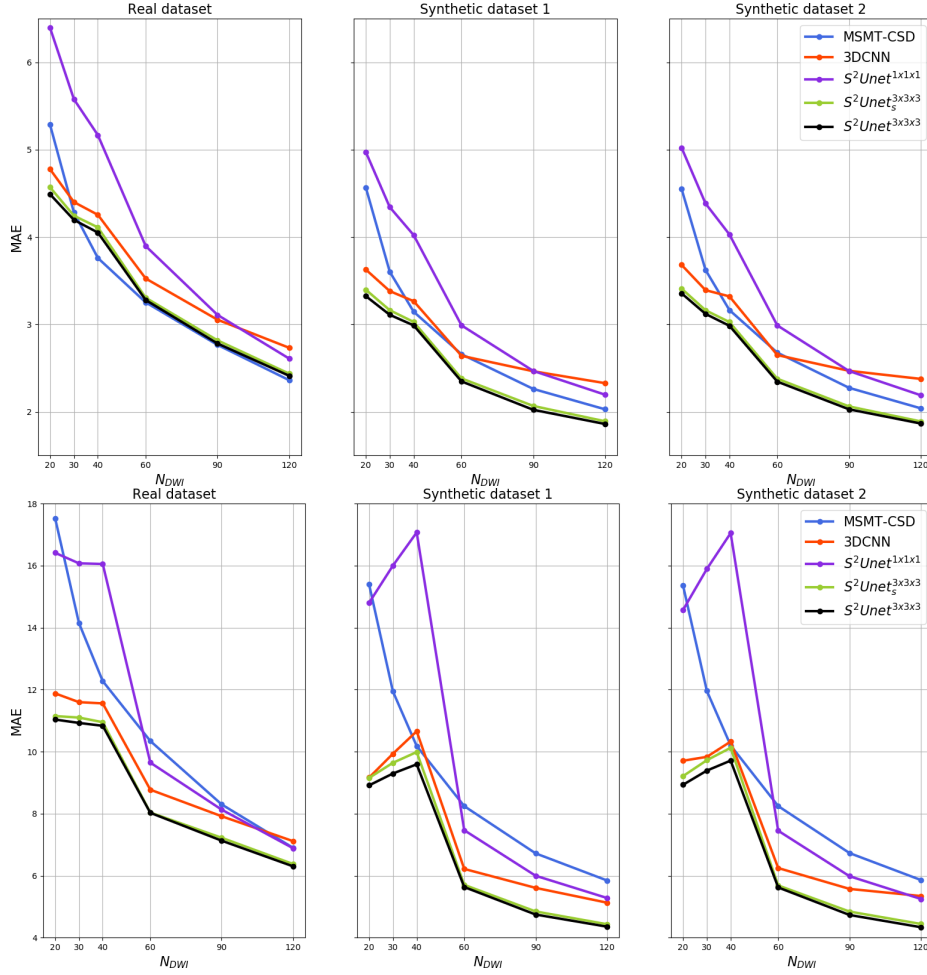


Fig. 3. Comparison of MAE averaged over 10 testing subjects for *real HCP dataset*, *Synthetic dataset 1* and *Synthetic dataset 2* for different number of sampling points for voxels containing single fibers (upper three sub-figures) and voxels containing two crossing fibers (lower three sub-figures)

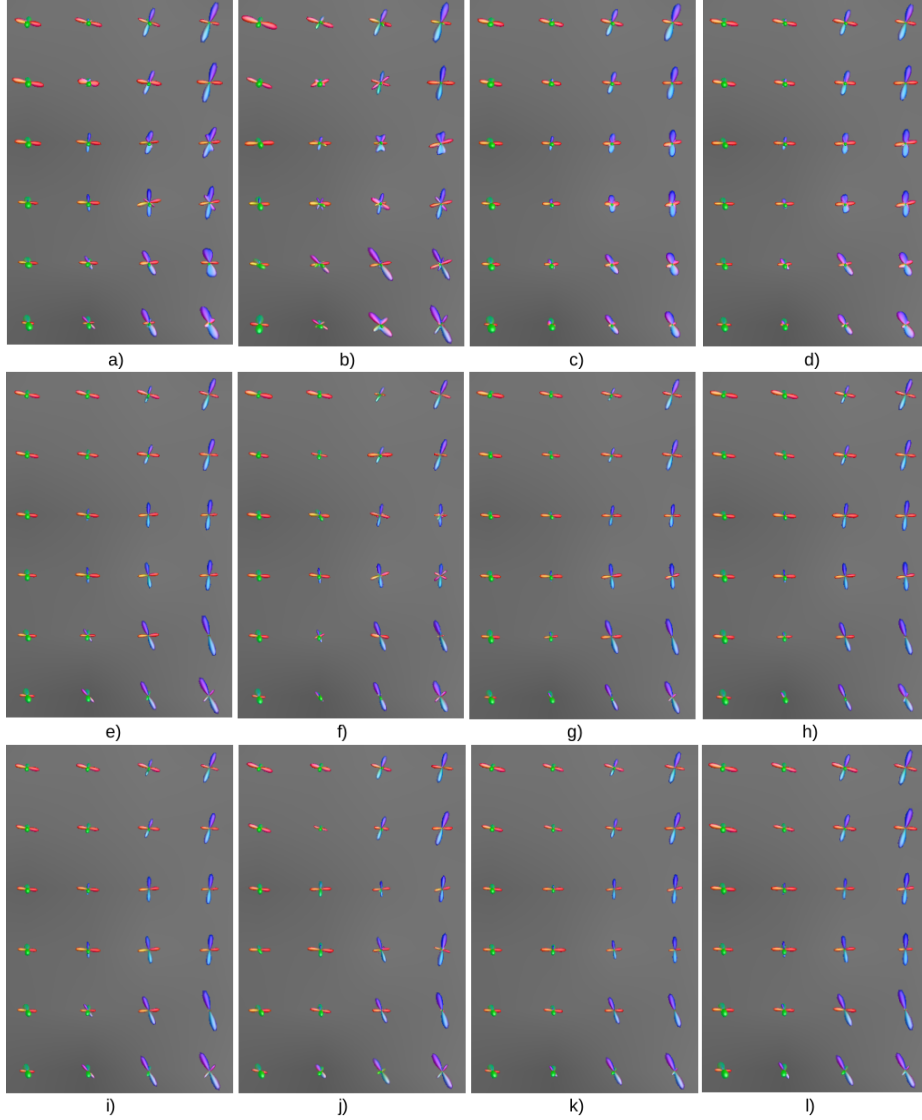


Fig. 4. Illustration of fODF gold standard and estimates obtained using MSMT-CSD, 3DCNN and $S^2U-net^{3 \times 3 \times 3}$ with angular resolution decreased to 60 points in total for the three shells. Sub-figures a), e) and i) correspond to the gold standard fODFs for *real HCP dataset*, *Synthetic dataset 1* and *Synthetic dataset 2*, respectively. Sub-figures b), f) and j) correspond to the fODF estimates obtained using MSMT-CSD; sub-figures c), g) and k) using 3DCNN and sub-figures d), h) and l) correspond to the fODF estimation with $S^2U-net^{3 \times 3 \times 3}$

6 Acknowledgment

This work was supported by the ERC under the European Union’s Horizon 2020 research and innovation program (ERC Advanced Grant agreement No 694665:CoBCoM : Computational Brain Connectivity Mapping).

This work has been partly supported by the French government, through the 3IA Côte d’Azur Investments in the Future project managed by the National Research Agency (ANR) with the reference number ANR-19-P3IA-0002.

Data were provided [in part] by the Human Connectome Project, WU-Minn Consortium (Principal Investigators: David Van Essen and Kamil Ugurbil; 1U54MH091657) funded by the 16 NIH Institutes and Centers that support the NIH Blueprint for Neuroscience Research; and by the McDonnell Center for Systems Neuroscience at Washington University.

The authors are grateful to Inria Sophia Antipolis - Méditerranée ”Nef” computation cluster for providing resources and support.

References

1. Le Bihan, Denis, et al. ”Diffusion tensor imaging: concepts and applications.” *Journal of Magnetic Resonance Imaging: An Official Journal of the International Society for Magnetic Resonance in Medicine* 13.4 (2001): 534-546.
2. Basser, Peter J., James Mattiello, and Denis LeBihan. ”MR diffusion tensor spectroscopy and imaging.” *Biophysical journal* 66.1 (1994): 259-267.
3. Wedeen, Van J., et al. ”Mapping complex tissue architecture with diffusion spectrum magnetic resonance imaging.” *Magnetic resonance in medicine* 54.6 (2005): 1377-1386.
4. Merlet, Sylvain L., and Rachid Deriche. ”Continuous diffusion signal, EAP and ODF estimation via compressive sensing in diffusion MRI.” *Medical image analysis* 17.5 (2013): 556-572.
5. Tuch, David S. ”Q-ball imaging.” *Magnetic Resonance in Medicine: An Official Journal of the International Society for Magnetic Resonance in Medicine* 52.6 (2004): 1358-1372.
6. Descoteaux, Maxime, et al. ”Regularized, fast, and robust analytical Q-ball imaging.” *Magnetic Resonance in Medicine: An Official Journal of the International Society for Magnetic Resonance in Medicine* 58.3 (2007): 497-510.
7. Tournier, J-Donald, et al. ”Direct estimation of the fiber orientation density function from diffusion-weighted MRI data using spherical deconvolution.” *Neuroimage* 23.3 (2004): 1176-1185.
8. Tournier, J-Donald, Fernando Calamante, and Alan Connelly. ”Robust determination of the fibre orientation distribution in diffusion MRI: non-negativity constrained super-resolved spherical deconvolution.” *Neuroimage* 35.4 (2007): 1459-1472.
9. Jeurissen, Ben, et al. ”Multi-tissue constrained spherical deconvolution for improved analysis of multi-shell diffusion MRI data.” *NeuroImage* 103 (2014): 411-426.
10. Basser, Peter J., et al. ”In vivo fiber tractography using DT-MRI data.” *Magnetic resonance in medicine* 44.4 (2000): 625-632.
11. Jbabdi, Saad, et al. ”Measuring macroscopic brain connections in vivo.” *Nature neuroscience* 18.11 (2015): 1546.

12. Lin, Zhichao, et al. "Fast learning of fiber orientation distribution function for MR tractography using convolutional neural network." *Medical physics* 46.7 (2019): 3101-3116.
13. Nath, Vishwesh, et al. "Deep Learning Estimation of Multi-Tissue Constrained Spherical Deconvolution with Limited Single Shell DW-MRI." arXiv preprint arXiv:2002.08820 (2020).
14. Ronneberger, Olaf, Philipp Fischer, and Thomas Brox. "U-net: Convolutional networks for biomedical image segmentation." *International Conference on Medical image computing and computer-assisted intervention*. Springer, Cham, 2015.
15. Zhao, Fenqiang, et al. "Spherical U-Net on cortical surfaces: methods and applications." *International Conference on Information Processing in Medical Imaging*. Springer, Cham, 2019.
16. Cohen, Taco S., et al. "Spherical cnns." arXiv preprint arXiv:1801.10130 (2018).
17. Esteves, Carlos, et al. "Learning so (3) equivariant representations with spherical cnns." *Proceedings of the European Conference on Computer Vision (ECCV)*. 2018.
18. Driscoll, James R., and Dennis M. Healy. "Computing Fourier transforms and convolutions on the 2-sphere." *Advances in applied mathematics* 15.2 (1994): 202-250.
19. Yeo, Boon Thye Thomas. "Computing spherical transform and convolution on the 2-sphere." Manuscript, MIT (2005).
20. Descoteaux, Maxime, et al. "Regularized, fast, and robust analytical Q-ball imaging." *Magnetic Resonance in Medicine: An Official Journal of the International Society for Magnetic Resonance in Medicine* 58.3 (2007): 497-510.
21. H. Rauhut, R. Ward, Sparse recovery for spherical harmonic expansions, arXiv preprint arXiv:1102.4097 (2011).
22. Van Essen, David C., et al. "The WU-Minn human connectome project: an overview." *Neuroimage* 80 (2013): 62-79.
23. Behrens, Timothy EJ, et al. "Probabilistic diffusion tractography with multiple fibre orientations: What can we gain?." *Neuroimage* 34.1 (2007): 144-155.
24. Wilkins, Bryce, et al. "Fiber estimation and tractography in diffusion MRI: development of simulated brain images and comparison of multi-fiber analysis methods at clinical b-values." *Neuroimage* 109 (2015): 341-356.
25. Smith, Stephen M., et al. "Advances in functional and structural MR image analysis and implementation as FSL." *Neuroimage* 23 (2004): S208-S219.
26. Zhang, Y. and Brady, M. and Smith, S. Segmentation of brain MR images through a hidden Markov random field model and the expectation-maximization algorithm. *IEEE Trans Med Imag*, 20(1):45-57, 2001.
27. J.-D. Tournier, R. E. Smith, D. Raffelt, R. Tabbara, T. Dhollander, M. Pietsch, D. Christiaens, B. Jeurissen, C.-H. Yeh, and A. Connelly. MRtrix3: A fast, flexible and open software framework for medical image processing and visualisation. *NeuroImage*, 202 (2019), pp. 116–37.
28. Emmanuel Caruyer, Christophe Lenglet, Guillermo Sapiro, Rachid Deriche. Design of multishell sampling schemes with uniform coverage in diffusion MRI. *Magnetic Resonance in Medicine*, Wiley, 2013, 69 (6), pp. 1534-1540. <http://dx.doi.org/10.1002/mrm.24736>
29. Abadi, Martín, et al. "Tensorflow: A system for large-scale machine learning." 12th USENIX symposium on operating systems design and implementation (OSDI 16). 2016.
30. Kingma, Diederik P., and Jimmy Ba. "Adam: A method for stochastic optimization." arXiv preprint arXiv:1412.6980 (2014).